Chandra and HST Observations of Radio-Selected (Wandering) Massive Black Hole Candidates in Dwarf Galaxies

MEGAN R. STURM, AMY E. REINES, ANNE M. LOHFINK, AKOS BOGDAN, RALPH KRAFT, DANIEL STERN, THOMAS CONNOR, JEREMY DARLING, AND MALLORY MOLINA

¹eXtreme Gravity Institute, Department of Physics, Montana State University, Bozeman, MT 59717, USA

²Center for Astrophysics | Harvard & Smithsonian, 60 Garden St., Cambridge, MA 02138, USA

³Jet Propulsion Laboratory, California Institute of Technology, 4800 Oak Grove Drive, Pasadena, CA 91109, USA

⁴Center for Astrophysics and Space Astronomy, Department of Astrophysical and Planetary Sciences, University of Colorado, 389 UCB, Boulder, CO 80309-0389, USA;

⁵ Vanderbilt University, 2201 West End Ave, Nashville, TN 37235

ABSTRACT

We present Chandra X-ray Observatory and Hubble Space Telescope (HST) follow-up observations of 12 dwarf galaxies from Reines et al. (2020) that are potential hosts of radio-selected active galactic nuclei (AGNs), eight of which are non-nuclear and possible "wandering" black holes (BHs). Our multi-wavelength analysis indicates a heterogeneous sample with five radio sources detected at both X-ray and optical wavelengths within positional uncertainties and non-detections for the remaining objects. Of the radio objects detected in the X-ray/optical, three have multi-wavelength evidence for hosting nuclear massive BHs and one object is consistent with an extreme compact starburst. Only one of the off-nuclear radio sources has a significant optical counterpart and we present Palomar spectroscopy that identifies this object as a background AGN. We cannot definitively determine if the seven remaining off-nuclear radio sources are wandering massive BHs in the target dwarf galaxies or background AGNs, although the three sources with the largest offsets have compact radio cores detected with the Very Large Baseline Array and are consistent with expectations for background AGNs (Sargent et al. 2022). Our HST sensitivity limits also allow for wandering massive BHs in the target dwarf galaxies that are hosted by stellar clusters with masses $\lesssim 10^6 M_{\odot}$.

Keywords: galaxies: active — galaxies: dwarf — galaxies: nuclei — X-rays: galaxies

1. INTRODUCTION

We observe supermassive black holes (BHs) in the centers of almost all massive galaxies (Magorrian et al. 1998) across the universe, however, their formation remains a mystery. Multiple potential mechanisms for supermassive BH seeding have been suggested including the collapse of Population III (PopIII) stars (Bond et al. 1984; Bromm & Larson 2004; Fryer et al. 2001; Haiman & Loeb 2001), the collapse of supermassive stars formed from massive gas clouds (Loeb & Rasio 1994; Begelman et al. 2006; Visbal et al. 2014; Habouzit et al. 2016), and a gravitational runaway event in a stellar cluster (Miller & Hamilton 2002; Portegies Zwart & McMillan 2002).

While BHs with $\sim 10^6 - 10^7 \,\mathrm{M}_\odot$ have now been observed at high-redshift with Chandra and JWST (Maiolino et al. 2024; Bogdán et al. 2024; Kovács et al. 2024), directly observing the first seed BHs ($\lesssim 10^5 \,\mathrm{M}_\odot$) remains out of reach (Volonteri & Reines 2016; Schle-

icher 2018; Vito et al. 2018). Each seeding model is expected to produce certain detectable signatures in $z \sim 0$ dwarf galaxies; therefore, combining observations of the high-z universe with observations of $z \sim 0$ dwarf galaxies in conjunction with semi-analytic models and simulations may allow us to identify the dominant seeding mechanism. Dwarf galaxies ($M_{\star} \lesssim 10^{9.5}~M_{\odot}$) provide a unique laboratory for studying BH formation and early evolution since they have relatively quiet merger histories compared to massive galaxies, meaning they can provide a 'fossil record' of the original BH seeds (Volonteri 2010).

For example, models of the BH occupation fraction and BH-galaxy scaling relations differ most substantially in the low-mass regime depending on the seeding mechanism (Volonteri et al. 2008; Volonteri & Natarajan 2009; van Wassenhove et al. 2010; Ricarte & Natarajan 2018). Additionally, dwarf galaxies host the smallest known supermassive BHs ($M_{\rm BH} \sim 10^{4-5}~M_{\odot}$), which places up-

per limits on the masses of BH seeds (for a review, see Reines 2022). Moreover, simulations indicate that as a result of supernova feedback stunting BH growth, dwarf galaxies should host relatively ungrown BHs (Anglés-Alcázar et al. 2017; Habouzit et al. 2017).

Since they emit observational signatures across the full electromagnetic spectrum (Ho 2008a), the vast majority of BHs found in dwarf galaxies are accreting and have been identified as active galactic nuclei (AGNs; e.g., Reines 2022; Salehirad et al. 2022; Pucha et al. 2025). Radio observations in particular are advantageous since AGNs, regardless of strength, almost always produce radio emission at centimeter wavelengths that is impervious to dust extinction. Additionally, observing high-energy X-ray point-like emission from a galaxy can be indicative of an accreting massive BH (Miller et al. 2015; Sacchi et al. 2024).

However, one complication in the dwarf galaxy regime is that candidate AGNs must be distinguished from potential extraneous sources due to star formation. Objects such as supernova remnants, young supernovae, and HII regions can produce emission in the radio, and some stellar-mass X-ray binaries can reach X-ray luminosities comparable to weakly accreting massive BHs. Since each wavelength regime involves different interloper sources that must be filtered out, multi-wavelength studies are a powerful tool for confirming the presence of AGNs (i.e., objects resembling an AGN at one frequency might not at other frequencies). Combining radio and X-ray observations is particularly useful for finding weakly accreting massive BHs in actively starforming dwarf galaxies (e.g., Reines et al. 2011, 2014). Moreover, high-resolution observations in the visible can help reveal optical counterparts of the radio/X-ray sources and provide details on the host galaxies (e.g., Kimbro et al. 2021).

In this work, we use a combination of X-ray and optical observations to further characterize the sample of radio-selected AGN candidates in dwarf galaxies from Reines et al. (2020). Reines et al. (2020) identify 13 objects that are detected as point-like radio sources at high angular resolution (~ 0.25) with the Karl G. Jansky Very Large Array and the sources are too luminous in the radio to be explained by normal star formation-related emission. The analysis of Reines et al. (2020) strongly argues against potential contamination sources including ionized gas from HII regions, supernova remnants (SNRs), younger radio supernovae (SNe), and stellar-mass X-ray binaries (XRBs), supporting the notion that these are truly AGNs.

A particularly unique quality of this specific sample is the fact that the compact radio sources do not always reside in the centers of their dwarf host galaxies. Instead, $\sim 70\%$ of them are offset from their host galaxy centers, with radio-optical positional offsets on the order of a couple of arcseconds ($\sim 1\text{-}2~\text{kpc}$). While this phenomenon of "wandering" black holes is quite unusual in the context of massive galaxies, it has been predicted in multiple simulations for dwarf galaxies hosting lowermass BHs ($M_{\rm BH} \sim 10^{4-6}~M_{\odot}$, Bellovary et al. 2010; Capelo et al. 2015; Tremmel et al. 2018a,b; Bellovary et al. 2019, 2021).

Dwarf galaxies generally have low central stellar densities and more irregularly shaped potential wells than their massive counterparts. For a small BH interacting with these kinds of systems, the dynamical friction timescales are much longer than the Hubble time (Taffoni et al. 2003; Ma et al. 2021; Bellovary et al. 2021), meaning that if a BH leaves the center of its host galaxy, it is unlikely to ever return. Consequently, when BH seeds either form outside of a galaxy center (Schneider et al. 2002) or, likely more often, when merger events involving tidal stripping (Bellovary et al. 2010; Tremmel et al. 2015) or gravitational slingshotting (Volonteri & Perna 2005; Merritt et al. 2004) occur, the result can be a large population of wandering BHs residing in the halos of their host galaxies. Bellovary et al. (2019) predicts that approximately half of all BHs in dwarf galaxies are wandering, with similar offsets as the Reines et al. (2020) sample. Despite their prevalence in simulations, wandering BHs remain observationally elusive. Follow-up work verifying the nature of the sample presented by Reines et al. (2020) is crucial because if the sources are truly AGNs associated with dwarf galaxies, they will provide concrete evidence in support of the theory of wandering BHs.

On the other hand, we cannot rule out the possibility that the radio sources from these putative wandering BHs may in fact be associated with background interlopers (i.e., AGNs) at $z \gg 0$. While Reines et al. (2020) present tentative evidence that the radio sources are associated with the dwarf galaxies rather than background AGNs based on enhanced [O I]/H α and [S II]/H α line ratios and statistical arguments using known cumulative radio source counts, further corroborating evidence is needed one way or the other. Some hints have come from follow-up Very Long Baseline Array (VLBA) observations. Sargent et al. (2022) observed the 13 radio AGNs associated with dwarf galaxies identified by Reines et al. (2020) and detected milliarcsecond-scale radio emission towards four of the targets (IDs 2, 28, 48, 65 in Reines et al. 2020) with brightness temperatures consistent with AGNs. However, these objects are the four most distant of the 13 VLA sources from the photocenters of their associated dwarf galaxies (2-4''), where the chance alignment with a background interloper is higher.

The VLBA nondetections of the other 9 VLA sources do not rule out the presence of AGNs (either in the associated dwarf galaxy or a background interloper); rather, the radio emission is likely resolved out given the dramatically increased angular resolution of the VLBA observations (Sargent et al. 2022). This type of partial resolution is a common phenomenon in radio AGNs (Deller & Middelberg 2014). Moreover, we have multiwavelength confirmation that two of the VLA radio sources not detected with the VLBA are indeed AGNs residing within the target dwarf galaxies. ID 26 is classified as an AGN based on its optical emission line ratios, broad H α emission (Reines et al. 2013), X-ray luminosity (Baldassare et al. 2017), and mid-IR colors (Latimer et al. 2021). ID 82 was confirmed by the AGN coronal line [Fe X], enhanced [O I] emission at the same location of the radio source and broad $H\alpha$ emission (Molina et al. 2021) 1 .

Here we continue our follow-up campaign of 12 objects from the Reines et al. (2020) sample of radio AGNs associated with dwarf galaxies. Our paper is primarily focused on new X-ray observations from the Chandra X-ray Observatory (Section 3) and optical imaging from the Hubble Space Telescope (HST, Section 4). In Section 5, we present the Palomar spectrum of one of our targets. We combine the pre-existing radio detections with our new X-ray, and optical detections/limits into a multi-wavelength view of this sample in Section 6. In this section, we also address the implications of our X-ray/optical non-detections and provide a detailed, multi-wavelength analysis of each object individually. We use a flat ΛCDM cosmology with $\Omega_{\rm m}=0.3$ and $H_0=73~{\rm km~s^{-1}~Mpc^{-1}}.$

2. SAMPLE OF DWARF GALAXIES WITH RADIO-SELECTED AGNS

The dwarf galaxies studied in this work are associated with candidate AGNs detected via luminous compact radio emission by Reines et al. (2020). In their study, Reines et al. (2020) start with the full NASA-Sloan At-

las (v0_1_2)², which is a catalog of SDSS galaxies with redshifts z < 0.055. They made cuts on stellar mass and absolute magnitude, requiring $M_{\star} \leq 3 \times 10^9 \ M_{\odot}$ (~the mass of the Large Magellanic Cloud) and M_q and $M_r >$ -20, which resulted in a parent sample of 43,707 dwarf galaxies. They cross-match this parent sample of dwarf galaxies with the VLA Faint Images of the Radio Sky at Twenty-centimeters (FIRST) Survey (Becker et al. 1995) catalog (version 2013 Jun 5). This resulted in 148 matches, which were targeted for further observations with the VLA at higher resolution (~ 0.25) and sensitivity (15 μ Jy). Ultimately, 111 of the targets were observed due to scheduling priorities. The new VLA observations have $\sim 20\times$ better angular resolution and $10\times$ the sensitivity of FIRST. Reines et al. (2020) detected compact radio sources towards 28 confirmed dwarf galaxies, 13 of which were compelling massive BH candidates based on radio luminosities exceeding that expected from starformation-related emission.

This paper is focused on 12 of these objects, for which we present Chandra and HST observations. We adopt the ID numbers used in Reines et al. (2020). Four of the dwarf galaxies have radio sources that are centrally located (IDs 26, 82, 83 and 92), while 8 radio sources are offset from the nuclei of the target galaxies (IDs 2, 6, 25, 28, 33, 64, 65 and 77). Properties of the 12 dwarf galaxies in our sample are summarized in Table 1. One galaxy from Reines et al. (2020), ID 48, is excluded from our follow-up observations since it lacks an SDSS spectrum and the radio source has a faint red optical point-source counterpart in DECaLS (Dark Energy Camera Legacy Survey; Dev et al. 2019) imaging, indicative that it is likely a background quasar. Moreover, Sargent et al. (2022) also detect the source with the VLBA and note that its distance from the center of the dwarf galaxy is consistent with expectations for a background AGN.

3. CHANDRA X-RAY OBSERVATIONS

X-ray observations of our target galaxies were taken with Chandra between 2014 December 26 and 2023 March 13, with exposure times ranging between 3.8 and 20.8 ks. We use archival Chandra data for two of our galaxies (IDs 26 and 92) and obtain new observations for our remaining 10 galaxies. In each observation the target galaxy was placed at the center of the ACIS-S3 chip, except for the archival observation of ID 92 (OB-SID 21518) in which the galaxy was placed at the aimpoint of the ACIS-I3 chip. A summary of the Chandra

 $^{^1}$ While the Si II $\lambda6371$ emission line has been misidentified as [Fe X] in some individual objects (e.g., Herenz et al. 2023), in the case of ID 82 the other line in the Si II doublet (Si II $\lambda6347)$ is clearly not present and, therefore, there is no reason to doubt the detection of [Fe X].

² http://nsatlas.org/

Table 1. Sample of Dwarf Galaxies with Radio Selected AGNs

ID	NSAID	SDSS Name	Radio RA	Radio DEC	$N_{ m H}$	z	Dist.	M_g	$\log(M_{\star}/M_{\odot})$
			(degrees)	(degrees)	$(10^{20} \text{ cm}^{-2})$		(Mpc)	(mag)	
(1)	(2)	(3)	(4)	(5)	(6)	(7)	(8)	(9)	(10)
2	26027	J001900.30+150710.9	4.74994	15.11973	3.57	0.03762	155	-18.42	8.6
6	23750	J010607.17 + 004633.6	16.53045	0.77620	2.39	0.01708	70	-18.42	9.4
25	26634	J090313.10 + 482415.5	135.80403	48.40381	2.29	0.02722	112	-17.46	8.8
26^a	10779	J090613.75 + 561015.5	136.55737	56.17087	2.52	0.04697	193	-18.98	9.4
28	12478	J090908.65 + 565522.1	137.28621	56.92215	3.10	0.03147	129	-17.46	8.3
33	16467	J093138.47 + 563319.0	142.91008	56.55552	2.77	0.04940	203	-16.72	8.3
64	66255	J113648.57 + 125239.7	174.20219	12.87775	2.83	0.03404	140	-18.63	9.3
65	101782	J113642.72 + 264337.6	174.17740	26.72657	2.11	0.03306	136	-18.27	9.2
77	3323	J120058.38 - 034116.3	180.24292	-3.68846	2.79	0.02570	106	-18.44	9.2
82^{b}	102751	J122011.25 + 302008.1	185.04694	30.33564	1.71	0.02690	110	-18.21	9.4
83	67389	J122603.63 + 081519.0	186.51518	8.25528	1.34	0.02409	99	-17.93	9.3
92	3602	J125305.97 - 031258.7	193.27487	-3.21632	1.50	0.02213	91	-19.99	8.6

NOTE—Column 1: Identification number assigned by Reines et al. (2020). Column 2: Identification number in the NSA. Column 3: SDSS name. Column 4: Compact radio source RA from Reines et al. (2020). Column 5: Compact radio source DEC from Reines et al. (2020). Column 6: Galactic neutral hydrogen column density (HI4PI Collaboration et al. 2016) c . Column 7: redshift, specifically the **zdist** parameter from the NSA. Column 8: Distance to galaxy. Column 9: absolute g-band magnitude corrected for foreground Galactic extinction. Column 10: log galaxy stellar mass. The values given in columns 9-12 are from the NSA and we assume h = 0.73.

observations is given in Table 2 and the observations can be found at 10.25574/cdc.367.

3.1. Chandra Data Reduction and Astrometry

We first reprocessed the data using CIAO software v4.16 (Fruscione et al. 2006) and applied calibration files (CALDB 4.11.5) to create new level 2 event files.

We then improve the Chandra absolute astrometry, which is typically good to $\sim 0\rlap.{''}4$. To achieve this, we began by creating an image in the broad ACIS energy band (0.5-7 keV) for each observation. Following this, we generated a list of detected X-ray point sources using the CIAO function wavdetect, excluding any sources that are detected with a significance of less than 3σ above the background or falling within $5\rlap.{''}$ of the target galaxy. The detected X-ray sources were matched to point sources in the Gaia DR3 catalog using the CIAO function wcs_match. We found several matching wavdetect and Gaia sources for each observation, and updated the Chandra astrometry using a translation

correction. The resulting geometric shifts are generally small (≤ 2 pixels) with the exception of OBSIDs 25271 and 25273 where unphysically large corrections were suggested by the software. Consequently, these two observations were not aspect corrected, however, they are also both non-detections with no possible targets within 5" of the target galaxies, making the lack of precision astrometry affect our results minimally, at most.

To find X-ray candidate sources, we re-run wavdetect after the astrometry correction unless multiple observations exist for the same target. Five of our target galaxies had multiple Chandra observations: ID 2 (OBSIDs 25269 and 26031), ID 6 (OBSIDs 2180 and 25270), ID 33 (OBSIDs 25273 and 26032), ID 64 (OBSIDs 24735 and 26181), and ID 65 (OBSIDs 25274, 26033, and 27940). These observations are merged prior to the final imaging analysis. We first merge the individually astromet-

^aThis object is also an optically-selected AGN with both AGN-like narrow-line ratios and broad Hα emission (ID 9 in Reines et al. 2013). It is also a mid-IR-selected AGN (ID 2 in Latimer et al. 2021).

^b This object also has optical AGN signatures, including the coronal line [Fe X], enhanced [O I] emission at the same location of the radio source, and broad Hα emission (Molina et al. 2021).

^cRetrieved via https://heasarc.gsfc.nasa.gov/cgi-bin/Tools/w3nh/w3nh.pl.

Table 2. Chandra X-ray Observations

ID	Date observed	Obs ID	Exp. time (ks)
2	2022 Sep 28	25269	16.84
2	$2022 \ \mathrm{Oct} \ 18$	26031	17.13
6	$2022~\mathrm{Jun}~12$	25270	7.95
6	$2001~{\rm Sep}~18$	2180	3.76
25	$2022~\mathrm{Jan}~26$	25271	16.73
26	$2014~{\rm Dec}~26$	17033	15.83
28	$2022~\mathrm{May}~28$	25272	18.12
33	$2022~{\rm Sep}~01$	25273	17.89
33	$2021~{\rm Dec}~08$	26032	20.76
64	$2021~\mathrm{Nov}~07$	24735	13.92
64	$2021~\mathrm{Nov}~08$	26181	13.93
65	$2022~\mathrm{May}~15$	26033	9.93
65	$2023~\mathrm{Jul}~05$	27940	8.28
65	$2023~\mathrm{Jul}~05$	25274	9.92
77	$2021~\mathrm{Apr}~15$	24736	17.88
82	$2022~\mathrm{Jul}~31$	25275	17.82
83	$2022~{\rm Feb}~27$	25276	14.86
92	$2019~{\rm Mar}~06$	21518	5.01

Note— New *Chandra* observations were taken for all galaxies except IDs 26 and 92, for which we use archival data.

rically corrected observations using the CIAO function merge_obs. Then, we run wavdetect on the merged images, similarly to our treatment of the individual images.

We restrict further analysis to $> 3\sigma$ detected sources within 5'' (i.e., a similar radius to the cross-matching radius used by Reines et al. 2020). Within such a radius at the depth of our X-ray observation, the chance of a background source is very low (Moretti et al. 2003) ³. This reveals candidate sources (distance to radio position < 5'') in IDs 26, 82, 83 and 92 (Figure 1). The detected X-ray sources are consistent with being central to the host galaxy, with the exception of ID 64 (likely a background AGN). Of the five galaxies requiring merging, one (ID 64) had detected sources in the galaxy region (this holds true in both the merged analysis and the analysis of the individual observations) at a significance of 3σ . We note here, that in ID 65, one observation had a tentative X-ray source detection (OBSID 27940) below our 3σ significance threshold; no source or hint of a source was detected in the other two observations of ID 65 (despite one been taken on the same day at similar depth).

Upon the successful detection of the X-ray source in ID 64, we checked the astrometric alignment of the unmerged images by comparing the centroids of the detected source in the unmerged OBSID event files. In ID 64, the astrometric offset between the two centroids was \ll 0".492 (one Chandra pixel), negating the need for further fine astrometric correction (see Figure 1). As such, no source centroids could be found, so no further astrometric corrections were applied.

3.2. X-ray Photometry

Our X-ray photometry builds upon the initial imaging results. In the case of a candidate source detection using wavdetect, we center our photometry on the coordinates identified by wavdetect. If no source is detected, we revert to using the original coordinates of the radio source for photometry. Source counts are extracted using the CIAO function srcflux, with circular apertures corresponding to the 90% enclosed energy fraction at 1.0 keV. To estimate the background counts, we use circular annuli centered on the source region, with an inner radius equal to 1.7× the radius of the source aperture and an outer radius set at 3× the source aperture radius.

The srcflux function is also used to calculate unabsorbed X-ray fluxes in the hard and soft energy bands. We adopt a power-law spectral model with a photon index $\Gamma = 1.8$, which is typical for both ultraluminous X-ray sources at these energies (Swartz et al. 2008) and low-luminosity AGNs (Ho 2008a, 2009). Galactic column densities are obtained from the maps of HI4PI Collaboration et al. (2016) and applied via the TBabs model (Wilms et al. 2000). In case of multiple observations, srcflux is run on the stack of all event files and the merged source fluxes are reported. If no source was detected, the srcflux returns estimates for the 90% confidence upper limits of net count rate and fluxes. The inferred 0.5–10 keV flux depends on the assumed spectral slope; varying Γ between 1.3 and 2.3 changes the flux estimate by roughly a factor of ~ 2.5 (0.4 dex), which represents the systematic uncertainty associated with the spectral assumption.

The net count rates, estimated unabsorbed fluxes, and luminosities are summarized in Table 3. The 2-10 keV luminosities range from $\log(L_{2-10\mathrm{keV}}/\mathrm{erg\,s^{-1}})=39.7-41.9$, assuming the sources reside within the target dwarf galaxies (see Table 3). These luminosity values should be considered as lower limits, as we do not account for potential intrinsic absorption by the sources. For observations where no X-ray sources are detected, we use estimated minimum detectable fluxes to establish upper limits on X-ray source luminosities.

 $^{^3}$ We also check if any of our sources are co-spatial with a source in the MILLIQUAS catalog (Flesch 2023) and do not find any such matches.

Table 3. X-ray Photometry

ID	R.A.	Decl.	R.A./Decl. error	Net Rate (10^{-4} cts/s)	Flux $(10^{-15} \text{ erg s}^{-1} \text{ cm}^{-2})$		Luminosity ($\log(\text{erg s}^{-1})$)	
	(deg)	(deg)	$(10^{-5}\deg)$	$0.5\text{-}10~\mathrm{keV}$	$0.5\text{-}2~\mathrm{keV}$	$2\text{-}10~\mathrm{keV}$	$0.5\text{-}2~\mathrm{keV}$	$2\text{-}10~\mathrm{keV}$
(1)	(2)	(3)	(4)	(5)	(6)	(7)	(8)	(9)
2^a				< 0.79	< 1.02	< 1.97	<39.5	<39.8
6^a				< 2.3	< 1.67	< 5.57	< 39.0	< 39.5
25				< 1.4	< 1.74	< 3.19	< 39.4	< 39.7
26	136.557593	56.170764	5.3/3.4	$8.7^{+4.5}_{-3.4}$	$4.40^{+2.51}_{-1.80}$	$2.51^{+4.80}_{-2.14}$	40.3 ± 0.2	$40.1_{-0.9}^{+0.4}$
28				< 1.3	< 1.56	< 2.96	< 39.5	< 39.8
33^a				< 1.0	< 0.86	< 0.27	< 39.6	< 39.1
64^a	174.202138	12.878138	0.8/0.9	$222.0{\pm}16.0$	$115.0^{+13.0}_{-12.0}$	$305.0^{+29.0}_{-30.0}$	41.4 ± 0.1^{b}	41.9 ± 0.1^{b}
65^{a}				< 3.3	< 2.88	< 5.32	< 39.8	< 40.1
77				< 1.3	< 1.52	< 2.96	< 39.3	< 39.6
82	185.047155	30.335761	10.0/7.6	$2.1_{-1.4}^{+2.4}$	< 2.76	$3.69_{-2.96}^{+4.92}$	< 39.6	$39.7^{+0.4}_{-0.3}$
83	186.514998	8.255182	1.3/1.2	$49.0_{-9.4}^{+9.5}$	$36.4^{+9.9}_{-8.5}$	$46.6^{+15.6}_{-12.7}$	$40.6 {\pm} 0.1$	$40.7^{+0.2}_{-0.1}$
92	193.274734	-3.216360	4.7/4.1	$23.2^{+13.4}_{-9.7}$	$17.6^{+14.1}_{-9.1}$	$24.6_{-14.7}^{+24.0}$	$40.2 {\pm} 0.3$	$40.4^{+0.2}_{-0.4}$

Note—Column 1: Identification number assigned by Reines et al. (2020). Column 2: right ascension of X-ray source. Column 3: declination of X-ray source. Column 4: uncertainties of X-ray coordinates. Column 5: net count rate after applying an aperture correction. Error bars represent 90% confidence intervals. Columns 6-7: fluxes corrected for Galactic absorption; calculated using a photon index of $\Gamma = 1.8$. Columns 8-9: photometric log luminosities corrected for Galactic absorption; calculated using a photon index of $\Gamma = 1.8$ and assuming the X-ray source is in the target dwarf galaxy. Log luminosities in the soft/hard band but calculated from the spectral modeling are: $40.9 \pm 0.2/39.0 \pm 0.4$ (ID 26), $41.47 \pm 0.03/41.86 \pm 0.03$ (ID 64), $40.7 \pm 0.1/40.8 \pm 0.1$ (ID 83), $40.4 \pm 0.2/40.8 \pm 0.2$ (ID 92).

3.3. X-ray Sources 3.3.1. Spectral Information

Spectroscopy provides deeper insights into the nature of the detected sources compared to photometry, and thus we created spectra for each of the five detected sources (see Figure 4 in Appendix A). We extract spectra using the CIAO task specextract using a circular source region centered on the source coordinates, while the background region is an annular area surrounding the source region. In the case of ID 64, the spectra obtained from the individual observations were combined to create a summed spectrum with corresponding responses using the task combine_spectra. All resulting spectra were then binned prior to modeling using grppha so that they possess a minimum of 1 count per bin (or 20 counts per bin in the case of ID 64). The spectra are modeled in the 0.5-10 keV range. As the spectrum of ID 64 is the only one with sufficient quality, it is modeled using χ^2 fitting while all other spectra are modeled using Cash statistics. Whenever possible, the absorption corrected fluxes were found using the cflux model, and

the corresponding luminosities can be found in Table 3. In the following, we briefly describe our X-ray spectral findings for each of the detected sources. All our spectral modeling was performed in XSPEC with spectral parameter uncertainties determined at the 90 % confidence level, using the error command. Galactic absorption is again described by the TBabs model.

ID 26: The spectral quality of the spectrum of ID 26 is poor especially at higher energies. The X-ray spectrum is very steep ($\Gamma = 5.1 \pm 1.4$) for a fit with a power law modified by Galactic absorption (N_H fixed). Although the spectral quality is poor, the spectrum is not quite consistent with a power law attenuated by Galactic absorption (best fit C-Stat= 17.8/13 dof), and visible residuals remain in the 0.8-1.0 keV range. If we replace the power law with the spectrum of a diffuse collisionally-ionized gas with solar abundances (XSPEC model apec), the residuals almost entirely vanish and the fit improves to C-Stat= 10.9/13 dof. The temperature of the plasma is found to be 0.5±0.3 keV, which is in line with what is commonly found for star-forming galaxies, see for example Kyritsis et al. (2025) for a re-

^aThese galaxies had multiple *Chandra* observations that required merging prior to analysis. Any coordinates listed are from the merged images; the merged count rate and fluxes are reported here (see Section 3.2).

 $[^]b$ If the X-ray emission originates from the background AGN at z=0.761 rather than the target dwarf galaxy (see Section 5), these luminosities would be 44.4 erg s⁻¹ in the 0.5-2 keV band and 44.9 erg s⁻¹ in the 2-10 keV band.

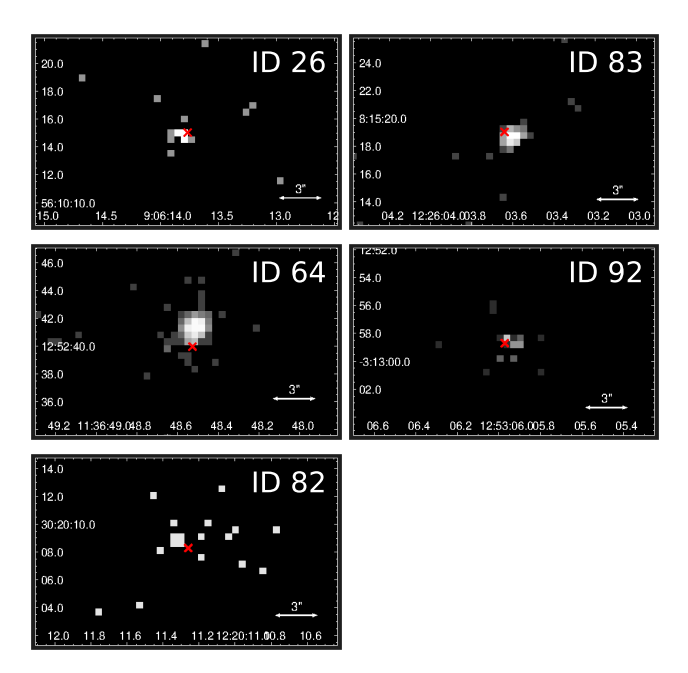


Figure 1. Chandra 0.5-7 keV images for our targets galaxies with X-ray detections. The red cross shows the locations of the detected compact radio sources. While the centroids of the Chandra sources do not always directly align, the sources are roughly positionally consistent.

cent example. As an alternative scenario, we attempted to free the column density in the absorbed power law scenario during the modeling to see whether the X-ray source could also be a slightly enshrouded, young, highly accreting, black hole but we found that such a model was not able to reproduce the 0.8-1.0 keV feature as well as the collisionally ionized plasma model.

ID 64: The summed X-ray spectrum of this target is consistent with a power law modified by Galactic absorption (best fit $\chi^2=25.5/28$ dof). Calculating the 1σ uncertainties in XSPEC we find the source to possess a fairly hard spectrum ($\Gamma=1.51\pm0.13$). There are no indications of any other components in the spectrum nor is intrinsic absorption indicated. We obtain the 2-10 keV flux from the power law component via the cflux model, finding $\log(f_{2-10\,\mathrm{keV}}/\mathrm{erg\,s^{-1}\,cm^{-2}})=-12.51\pm0.05$.

As we discuss in section 6.5, it is quite likely that this source is in fact a background AGN at redshift 0.761. If true, then the modeled 0.5-10 keV band would correspond to an actual intrinsic energy range of \sim 0.9 – 17.6 keV. Within this energy band, intrinsic absorption cannot be ruled out at the same level of confidence, however absorption in excess of $N_H = 10^{22} {\rm cm}^{-2}$ is not consistent with the observed spectrum. Such as background AGN would have a 2 – 10 keV luminosity of approximately $7 \times 10^{44} {\rm erg/s}$.

ID 82: ID 82 has low photon count and a usable spectrum can therefore not be extracted. Nevertheless, we have some spectral information in that the target is only detected at hard energies. This could be suggestive of an obscured accreting black hole. Using the WebPIMMS v4.51 tool to estimate how much absorption is consistent with the observed fluxes, we find that a column of a few $\times 10^{21} \, \mathrm{cm}^{-2}$ is consistent with our findings, assuming the spectrum can be roughly described as an absorbed power law with a photon index in the range of 1.8-2.2.

ID 83: The spectrum of ID 83 is statistically consistent with a power law modified by Galactic absorption (C-Stat=58.9/61 dof). The photon index derived from such a description of the data is 2.0 ± 0.4 .

ID 92: Due to the extremely short exposure time of only 5 ks, the spectrum of ID 92 is very poor. It is very well described by a power law modified by Galactic absorption (C-stat= 11.9/16). The constraining power of the spectrum is minimal and therefore the power law photon index is poorly constrained to 1.4 ± 0.7 .

3.3.2. Expected Contribution from Ultraluminous X-ray Sources

Our high-resolution Chandra observations reveal Xray sources toward five of our target dwarf galaxies with luminosities of $L_{2-10 \text{ keV}} \sim 10^{40-42} \text{ erg s}^{-1}$. If the X-ray and radio emission originate from the same object, the high radio luminosities provide strong evidence for AGNs as the origin, as stellar-mass objects have much lower ratios of radio to X-ray emission. However, if the radio and X-ray emission originate from separate objects, which is possible given the astrometric uncertainties, it is possible that ultraluminous X-ray sources (ULXs), generally defined to be off-nuclear Xray sources with $L_{\rm X} > 10^{39} {\rm erg \ s^{-1}}$ (Kaaret et al. 2017), could be responsible for the observed X-ray luminosities. Therefore, we assess the likelihood of ULXs here using the relation in Lehmer et al. (2021) between the number of ULXs expected in a galaxy based on the star formation rate (SFR) and gas-phase metallicity.

We estimate SFRs for our target dwarf galaxies using far-UV (FUV; 1528 Å) and mid-infrared (IR; 25 $\mu m)$ luminosities:

$$\log SFR(M_{\odot} \text{ yr}^{-1}) = \log L(FUV)_{\text{corr}} - 43.35$$

$$L(FUV)_{\text{corr}} = L(FUV)_{\text{obs}} + 3.89L(25 \ \mu\text{m})$$
(1)

(Hao et al. 2011; Kennicutt & Evans 2012), where the uncertainty for the estimated SFR is \sim 0.13 dex. We retrieve FUV magnitudes from the *Galaxy Evolution Explorer* (*GALEX*), and for the IR data use 22 μ m magnitudes from the *Wide-field Infrared Survey Explorer*

(WISE) instead of 25 μ m magnitudes from the Infrared Astronomical Satellite (IRAS). None of our galaxies are detected by IRAS, while all twelve have WISE detections, and the ratio between 25 μ m and 22 μ m flux densities is expected to be \sim 1 (Jarrett et al. 2013). As discussed in Latimer et al. (2021), ID 26 is a mid-IR-selected AGN, implying the UV+IR SFR is likely severely overestimated due to AGN emission at mid-IR wavelengths. Therefore, we adopt the uncorrected UV SFR of 0.14 $M_{\odot}/\rm yr$ from that work. The resulting SFRs for the five galaxies with X-ray detections are 0.14, 0.34, 0.29, 0.16 and 10.49 M_{\odot} yr⁻¹ for IDs 26, 64, 82, 83, and 92, respectively.

Following Latimer et al. (2021), we estimate the metallicities of our dwarf galaxies based on the ratio of [N II]/ H α as calculated in Reines & Volonteri (2015) and the relation given in Pettini & Pagel (2004). The metallicities of the galaxies, excluding ID 92, range from $12 + \log(\mathrm{O/H}) = 8.46\text{-}8.66$ with a mean of 8.55. We are unable to include ID 92 in this calculation due to the poor quality of the SDSS spectrum. From the relation derived in Lehmer et al. (2021, see their Figure 6) we expect \sim 0.1 and ULX with $L_{\rm X} > 10^{40}$ erg s⁻¹ per unit SFR at a metallicity of $12 + \log(\mathrm{O/H}) = 8.5$. Given the total SFR for these four galaxies is $0.93~M_{\odot}/\mathrm{yr}$, the expected number of ULXs is $\lesssim 0.1$. Therefore, it is likely that the detected X-ray sources in these four galaxies are due to AGNs.

ID 92 is a blue compact dwarf galaxy and is in the sample studied by Thuan & Izotov (2005). They find $12 + \log(O/H) = 8.05$ and we expect ~ 0.2 ULX with $L_{\rm X} > 10^{40}$ erg s⁻¹ per unit SFR at this lower metallcity (Lehmer et al. 2021). Therefore, ID 92 may have 2 ULXs given its relatively high SFR and the presence of a massive star forming region seen in HST imaging (see Section 6.5).

4. HST OPTICAL OBSERVATIONS

Our new HST optical images were taken between 23 November 2021 and 25 April 2022 in two programs (program IDs 16661 and 16843) using the Wide Field Camera 3 (WFC3) UVIS imaging instrument. We observed each galaxy for one orbit in three filters. We used a narrow-band ${\rm H}\alpha$ filter (either F665N or F680N, depending on the redshift of the target galaxy) and two wideband filters including F814W (centered at 8039Å) and either F438W or F475W (centered at 4326Å or 4773Å, respectively).

For program ID 16843, each galaxy was observed in one orbit with exposure times of \sim 17-20 minutes in the narrow-band H α filter and \sim 9-12 minutes in the wide-

Table 4. HST Observations

ID	Program ID	Date observed	Exp. tin	Exp. time (s) in each		
			F475W	F680N	F814W	
2	16843	2021 Dec 05	584	1060	600	
25	16843	$2022~\mathrm{Jan}~09$	600	1172	600	
28	16843	$2021~{\rm Dec}~31$	636	1120	720	
33	16843	$2022~{\rm Feb}~13$	626	1120	720	
65	16843	$2021~{\rm Dec}~30$	584	1060	608	
82	16843	$2021~{\rm Dec}~27$	584	1060	624	
83	16843	$2022~\mathrm{Jan}~02$	532	1030	570	
			F475W	F665N	F814W	
6	16843	2021 Dec 27	574	1060	600	
			F438W	F680N	F814W	
64	16661	2022 Apr 25	810	2391	996	
77	16661	$2021 \ \mathrm{Nov} \ 23$	810	2385	990	
92	16661	$2022~\mathrm{Jan}~06$	810	2382	987	
			F275W	F606W	F110W	
26	13943	2015 Feb 18	900	648	514	

Note—New HST observations were taken for all of the galaxies in our sample except ID 26, for which we use archival HST imaging. Our HST observations can be found at 10.17909/h9mh-tg88.

band filters. For program ID 16661, each galaxy was observed over two orbits for ~ 40 minutes in the narrowband H α filter and $\sim 13\text{-}17$ minutes in the wide-band filters. For ID 26 we use archival data from program ID 13943 (PI Reines) from 18 February 2015. The galaxy was observed in three wide-band filters: for 15 minutes in the F275W filter (centered at 2710Å), for 10 minutes in the F606W filter (centered at 5889Å) and for 8.5 minutes in the IR F110W filter (centered at 1153Å). A summary of the HST observations is given in Table 4 and the observations can be found at 10.17909/h9mhtg88.

4.1. HST Data Reduction and Astrometry

We obtained the calibrated and drizzled Hubble Advanced Product (HAP) Single Visit Mosaics (SVMs) produced by the STScI data reduction pipeline. The HAP SVMs are drizzled onto the same north-up pixel grid and are aligned to a common astrometric reference frame. The pipeline attempts to improve both the relative astrometry between filters as well as the absolute astrometry by aligning sources in the images to the *Gaia* source catalog.

Table 5. Optical Photometry

ID	F275W	F438W	F475W	F606W	F665N	F680N	F814W	F110W
2	• • •		>24.34			>24.50	>24.79	
6			> 23.71		> 23.83		>24.08	
25			> 23.29			> 23.53	> 23.73	
26	20.23			20.03				21.28
28			>24.04			>24.28	>24.50	
33			>24.22			>24.13	>24.62	
64		21.19				21.74	21.86	
65			>24.03			>24.10	>24.22	
77		> 22.84				> 23.03	> 23.28	
82			20.30			20.19	21.12	
83			20.42			20.20	20.42	
92		17.24				16.74	18.76	

Note—Optical ST magnitudes in each filter measured from photometry at the location of the compact radio source for galaxies in our sample. If the flux within an aperture with radius 0'.'2 exceeds the background flux by 3σ , we report the detected magnitude. In the case that the flux does not exceed 3σ of the background we report a lower limit on the magnitude (upper limit on the brightness) of the non-detection. An ellipses indicates that the target was not observed with that specific filter.

When necessary, we made additional fine adjustments to the astrometry in each of our images by comparing common sources with DECaLS, which has absolute astrometry accurate within $\sim 0.1^{\circ}$. We shifted each SVM image individually to match the DECaLS images and then updated the WCS for our images accordingly. The resulting astrometric corrections had a maximum RA shift of 0.39 and a maximum DEC shift of 0.39.

4.2. Optical Photometry

For a given galaxy, we perform aperture photometry in the regions around the detected radio source to determine if there is detectable emission (i.e., an optical counterpart) in each band. We search for optical counterparts located within 0".25 of the radio source, which is equivalent to the resolution of the VLA observations presented in Reines et al. (2020). This search radius also allows for uncertainties in the absolute astrometry between the VLA and HST observations (~ 0.11 each). We perform aperture photometry on identifiable sources using a source aperture of 0".2 centered on the optical source and a nominal background annulus with an inner radius of $r_{in} = 0.3$ and outer radius of $r_{out} = 0.4$. Since the uncertainty associated with this measurement is dominated by the background, we vary the background annulus and find an average error of \sim 6%. Aperture corrections were applied to our final background-subtracted flux densities using the appropriate encircled energy fractions for a 0"2 aperture. To ensure solid detections, we also require the backgroundsubtracted source flux density to be larger than 3σ above the median background. In cases where there is no obvious optical counterpart, we derive upper limits by performing aperture photometry using the same method described above but with the aperture centered on the radio source. The measured values and upper limits are given in Table 5.

We find five galaxies (IDs 26, 64, 82, 83 and 92) that have significant optical detections at the location of the radio source in all of their filters. These same five galaxies also have overlapping Chandra X-ray detections (see Figure 3 and Table 7). Four of the radio sources with optical detections are located in the nuclei of their host dwarf galaxies, while the remaining radio source in ID 64 is off-nuclear and our Palomar spectroscopy of the relatively bright optical counterpart reveals that it is a background AGN (see Section 5).

5. PALOMAR SPECTROSCOPY OF ID 64

The radio source in ID 64 is of particular interest since it is the only off-nuclear source in our sample that has a bright optical counterpart, and, therefore, we elected to take further observations of this object. On the night of UT 2021 December 5, we obtained a single 1200 s exposure of ID 64 with the Double Spectrograph on the Palomar 5-m Hale Telescope. The night was photometric and the seeing was 1.75 at the time of the observation. The instrument was configured with a 1.75 wide slit, which was oriented at a position angle of 109° east of north in order to simultaneously observe both the

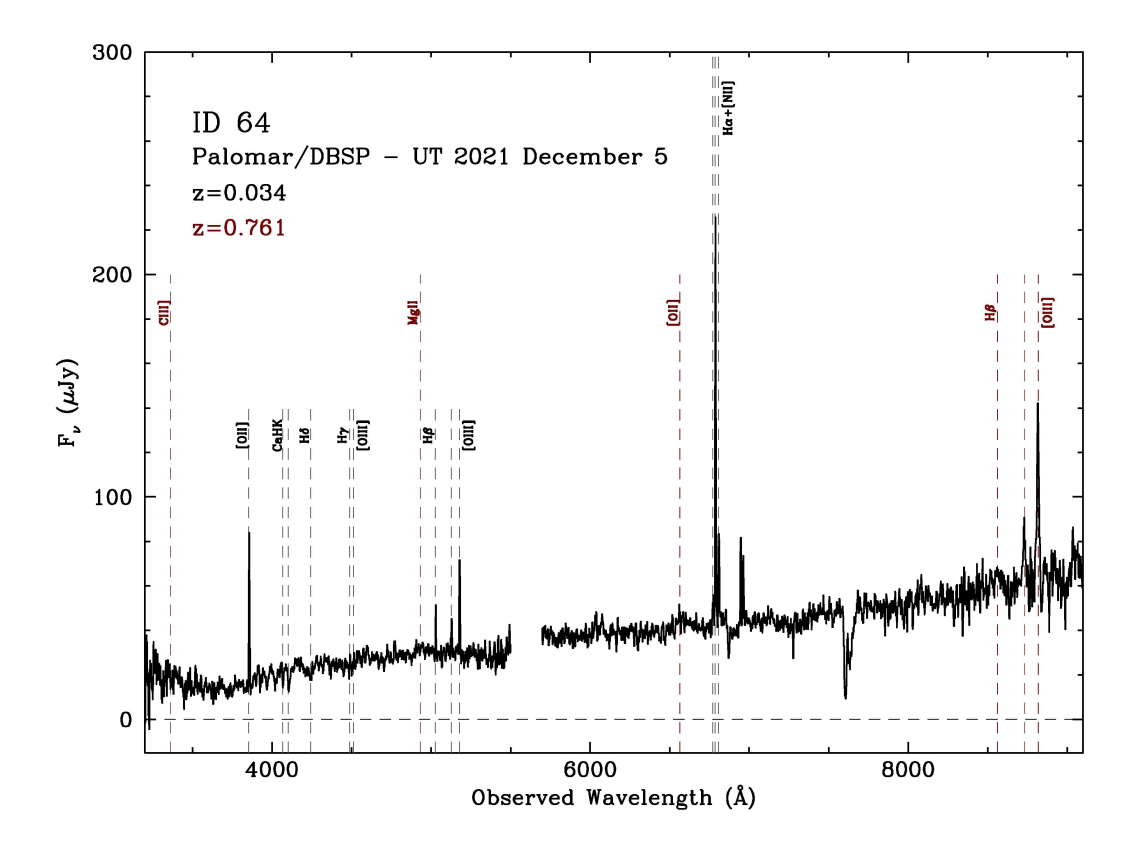


Figure 2. Palomar Double Spectrograph (DBSP) spectrum of the bright optical counterpart to the radio source in ID 64. Foreground narrow emission lines in the dwarf galaxy are marked in black and correspond to a redshift of z = 0.034. There is another set of emission lines shown in red that correspond to a redshift of z = 0.761 and that likely originate from a background AGN associated with the radio source.

central region of the dwarf galaxy and the offset point source to the west that is spatially coincident with the radio source.

We processed the data with IRAF using standard techniques and flux-calibrated the spectrum using standard stars observed on the same night. The reduced spectrum (shown in Figure 2) reveals multiple narrow emission lines from the dwarf galaxy at z = 0.034, consistent with star formation. Several of the emission lines are spatially extended, and we also detect absorption lines and a Balmer decrement consistent with star formation in the dwarf galaxy. In addition, we detect two slightly broader lines redwards of 8500 Å which are identified as the [O III] doublet at z = 0.761. The lack of associated $H\beta$ emission implies a high-ionization source with log [O III] $5007/H\beta \gtrsim 1$; i.e., an active galaxy according to the Baldwin, Phillips & Terlevich (BPT) diagram (Baldwin et al. 1981). The lack of associated strong broad lines suggest that the interloper active galaxy is obscured.

6. A MULTI-WAVELENGTH VIEW

In the initial radio study conducted by Reines et al. (2020), through a detailed analysis calculating the expected emission at 9 GHz from various potential stellar sources within the dwarf galaxies (supernovae, supernovae remnants and thermal HII regions), our 12 galaxies were found to have luminosities brighter than what any of these stellar sources could likely produce. Therefore, Reines et al. (2020) conclude that these objects are very likely to be AGNs, either within the host dwarf galaxy or background objects. We combine this work at radio wavelengths with our new X-ray and optical data to further characterize the sources of the compact radio emission.

⁴ Reines et al. (2020) notes that, taking into account the uncertainties, the luminosity for ID 92 is consistent with an HII region with an instantaneous star formation rate equivalent to that expected for the entire galaxy.

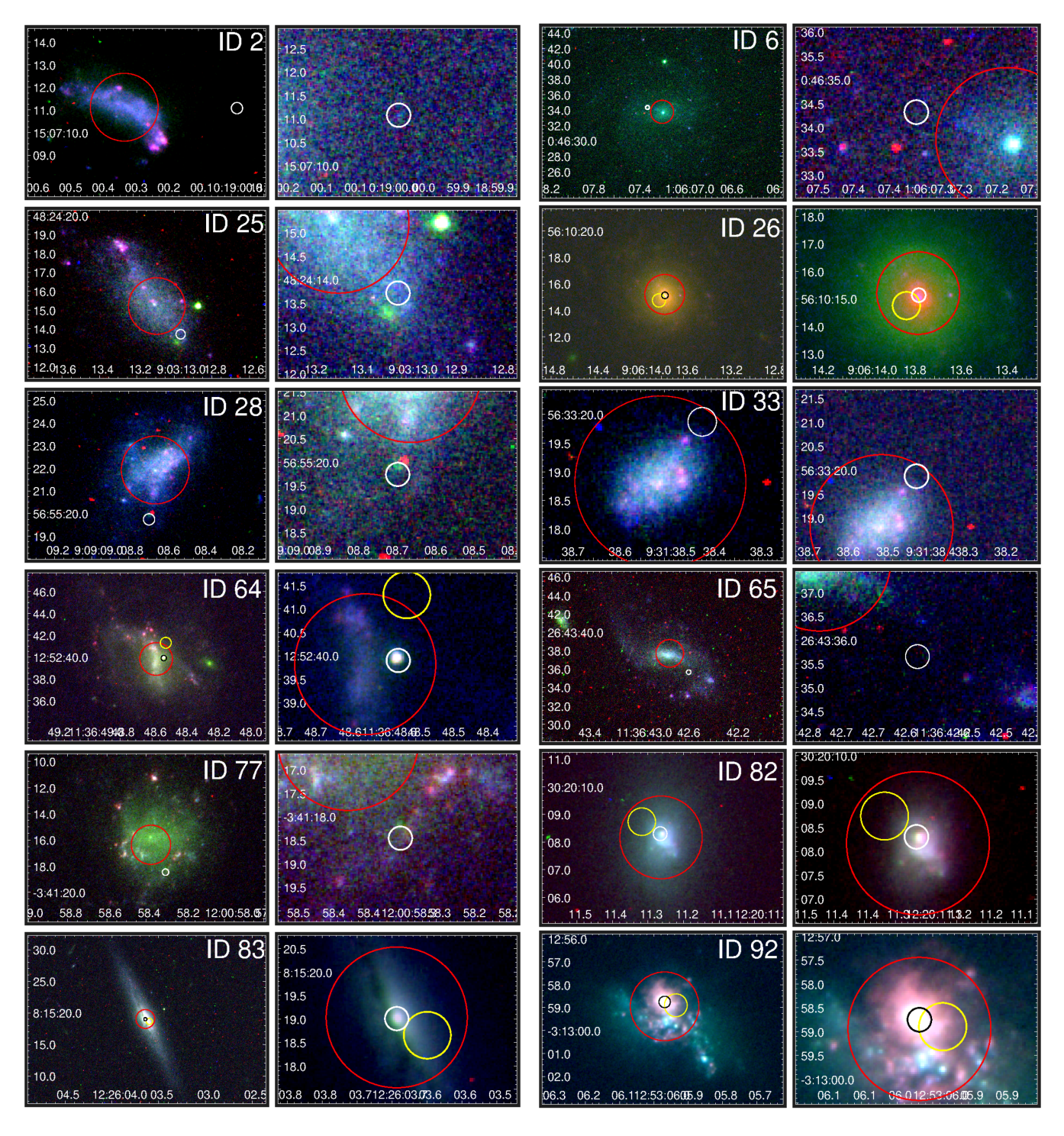


Figure 3. Three-color HST images of our galaxies. Green corresponds to the wide I-band F814W filter or wide YJ F110W filter (for ID 26), red corresponds to the H α F680N or F665N filter (for ID 6) or wide V-band F606W filter (for ID 26) and blue corresponds to the wide B-band F475W or SDSS g-band F438W filter (for IDs 64, 77 and 92) or wide UV F275W filter (for ID 26). The white/black circles have radius 0.25 and show the location of the compact radio source. The yellow circles show the location of the X-ray detections with radii 0.55. The red circles indicate the location of the SDSS fibers with diameter of 3.50. IDs 26, 64, 82, 83 and 92 all have both optical counterparts to the radio sources observed in all filters and X-ray detections corresponding to roughly same sky location (also see Figure 1).

6.1. Radio Source Positions and their X-ray and Optical Counterparts

Figure 3 shows HST three-color images for our sample of dwarf galaxies. The locations of the radio sources are marked with white or black circles with radii of 0".25 (i.e., the resolution of the VLA observations). We also mark the positions of the X-ray sources for the five galaxies with detections using yellow circles with radii of 0".5.

We find five galaxies in our sample with significant X-ray and optical counterpart detections: IDs 26, 64, 82, 83 and 92. All five of these detections have X-ray source positions that are roughly consistent with the positions of the radio sources (see Figure 1) and are unlikely to be background X-ray sources aligning with our target galaxies by chance (Moretti et al. 2003; Flesch 2023). Besides the background AGN residing in ID 64 (see §5), the rest of these galaxies have radio/optical/X-ray sources consistent with the center of the dwarf host galaxies. The remaining seven galaxies, which all have off-nuclear radio sources, do not have significant optical or X-ray counterparts. We discuss the implications of the optical and X-ray non-detections in Section 6.4.

6.2. X-ray Radio-Loudness

The X-ray radio-loudness parameter (R_x) is defined as the ratio of radio luminosity (at 5 GHz) to the hard Xray luminosity (from 2-10 kev), with $\log R_x > -4.5$ being considered "radio-loud" (Terashima & Wilson 2003; Ho 2008b). We calculate this parameter for the five galaxies in our sample with overlapping X-ray and radio detections, assuming that the sources of the X-ray and radio emission are the same. We use the X-ray luminosities from §3.3 and estimate 5 GHz radio luminosities using the 9 GHz flux densities and spectral indices from Reines et al. (2020). We find values in the range $-3.9 \le$ $\log R_x \leq -1.7$ and these objects are therefore considered radio-loud. We calculate uncertainties on the X-ray radio loudness parameter by propagating the errors on the measured X-ray fluxes and the errors reported by Reines et al. (2020) for S_{9GHz} and α . Uncertainties for L_{5GHz} are $\sim 20\%$ and uncertainties for R_X range from 4%-30% with one outlier (ID 25) at 60%. Lower limits on R_x are calculated for the radio sources without X-ray detections. The R_x values are given in Table 6.

For comparison, the low-luminosity AGNs in the dwarf galaxies Henize 2-10 and Mrk 709 have $\log R_x = -2.4$ (Reines et al. 2016) and -3.7 (Reines et al. 2014), respectively. The Terashima & Wilson (2003) sample of optically-selected, low-luminosity AGNs (LLAGNs), originally from the Palomar survey of bright objects (Ho et al. 1995) and also observed in the radio (Na-

gar et al. 2000), have X-ray radio-loudness values in the range $-4.6 < R_X < -1.2$. The X-ray radio loudness values we find for our sample lie within this range. Additionally, the low-mass AGNs studied in Gültekin et al. (2022) have X-ray radio-loudness values in the range $-5.3 \lesssim R_X \lesssim -1.4$. The eight AGNs from Gültekin et al. (2022) were originally selected as AGNs by Reines et al. (2013) based on their optical narrow emission line ratios and broad H α emission. These objects then had follow-up X-ray (Baldassare et al. 2017) and radio observations (Gültekin et al. 2022). Given that the objects studied here were originally selected in the radio, it is not surprising that our sample generally has relatively high R_X values compared to optically-selected samples of AGNs.

6.3. Optical Radio-Loudness

The optical radio-loudness parameter (R) describes the ratio of the luminosity density (with units of erg $s^{-1} Hz^{-1}$) in the radio (at 5 GHz) to the optical (4400 Å, Kellermann et al. 1989), with R>10 being considered "radio-loud." Again, we estimate 5 GHz radio luminosities using the 9 GHz flux densities and spectral indices from Reines et al. (2020). We estimate the luminosity density at 4400 Å through a linear interpolation in log space between the flux density measurements (or upper limits) in the shortest and longest wavelength filters. We report the radio-loudness parameter (and lower limits in the case of no detection in the optical images) for galaxies in our sample in Table 6. Our radio sources are almost all considered radio-loud, with only ID 92 having $\log R < 1$. We estimate uncertainties on the optical radio loudness parameter by propagating the errors on the measured optical fluxes (see Section 4.2) and the errors reported by Reines et al. (2020) for S_{9GHz} and α . Uncertainties for L(5GHz) are $\sim 20\%$ (as in Section 6.2), uncertainties for L(4400 Å) are \sim 6% and uncertainties for R are $\sim 15\%$.

We find that the optical radio-loudness values are within the typical range of known radio-loud quasars. We recalculate our radio-loudness parameters (and corresponding uncertainties) using the method described above, but at 2500 Å for consistency with the work done by Miller et al. (2011) and Shen et al. (2011, , this parameter is referred to as R* in Miller et al. (2011), with R* > 10 considered radio-loud). Shen et al. (2011) reports values for all quasars from SDSS DR7 and Miller et al. (2011) reports values for radio-loud quasars from SDSS DR5. Both samples were mostly optically-selected using the corresponding SDSS Quasar Catalogs (Schneider et al. 2007, 2010). Miller et al. (2011) also uses a photometric sample of optically-selected AGNs based on

Richards et al. (2009) classification and a "quasi-radio-selected" sample, which consists of objects originally targeted by SDSS as potential optical counterparts to FIRST sources. For both these samples, log R values range from ~ -0.6 to 5, with our sample falling within this range. We note that extrapolating linearly in log-log space to find the flux density at 2500 Å is less reliable than extrapolating to 4400 Å given the filters used for our observations, as uncertainties for L (2500 Å) are $\sim 7\%$ and uncertainties for R* are $\sim 20\%$. However, since we are calculating log R, the difference between our extrapolated flux density and the true value likely has a small impact.

6.4. Implications of Optical/X-ray Non-detections

Seven galaxies in our sample do not have significantly detected optical counterparts in the HST imaging at the locations of the radio sources, all of which are spatially offset from the centers of the dwarf galaxies. Here we consider the implications of these non-detections.

If the radio-detected AGNs are wandering BHs in the dwarf host galaxies, they may be isolated BHs without a stellar counterpart, possibly accreting from either the ISM or a retained accretion disk (Bonning et al. 2007; Blecha et al. 2011), and we would not detect an optical source. Alternatively, the BH may be surrounded by a stellar cluster that we could potentially detect. We use our derived upper limits in the HST imaging to constrain the properties of a putative detectable star cluster. We model a star cluster in each galaxy using the GALEV simple stellar population (SSP) synthesis model (Kotulla et al. 2009), with Padova isochrones, a timestep of 4 Myr, a Kroupa initial mass function (IMF) spanning $0.1 - 100 M_{\odot}$, and a metallicity of [Fe/H] = -0.7. We take this model at ages 10 Myr, 100 Myr, and 1 Gyr and scale the spectra given the redshift of each galaxy. We convolve this GALEV model with the F814W filter throughput curve to determine a model flux density in this band. Assuming the flux density scales linearly with the mass of the star cluster, we calculate the upper limit range⁵ on the possible mass of a cluster that we would not be able to detect at optical wavelengths. We find that a cluster at 10 Myr would be below our detection limits if it had log $(M/M_{\odot}) \lesssim 5.0$ -5.7, while the older clusters could be even larger with $\log (M/M_{\odot}) \lesssim 5.8$ -6.5 and log $(M/M_{\odot}) \lesssim$ 6.3-7.0, for 100 Myr old and 1

Gyr old clusters, respectively. These are typical masses for globular and nuclear star clusters, and, therefore, it remains a possibility that there are star clusters hosting wandering BHs in these dwarf galaxies that are below our detection limits. With deeper *JWST* observations, we would ideally be able to observe the potential star clusters accompanying these radio sources.

Additionally, as exemplified by ID 64 (§5), it is possible that these radio sources are not associated with the dwarf galaxies at all and instead are background interlopers that happen to overlap with our galaxies in the sky. We consider possible galaxy hosts at various redshifts to derive upper luminosity limits on potential AGN host galaxies that would be below our optical detection limits. We use the flux density limits for our nondetections and calculate the luminosity in the F814W filter (roughly I-band) at various redshifts. We find that the putative host galaxies would have $\log(L/L_{\odot}) \lesssim 9.1$, 9.8, 10.6, and 11.0 for z=0.5,1,2 and 3, respectively.

We now consider the X-ray non-detections. Seven of the radio sources do not have detectable X-ray counterparts. These sources tend to have relatively high upper limits on their X-ray radio loudness parameters (see Table 6), i.e., they are under-luminous in the X-ray band. One potential explanation is that some of the AGNs in these objects, e.g., IDs 6 and 65, are highly obscured in the X-ray band. For example, if ID 6 was obscured by a column density of $\gtrsim 10^{24} \, \mathrm{cm}^{-2}$, it could hide an AGN with $\log(L_{2-10\,\mathrm{kev}}) \sim 40.7 \mathrm{\ erg\ s^{-1}}$. It is also possible that the AGN emission has changed, as the radio and X-ray observations are non-simultaneous; in this case, the sources could be "changing-look" AGNs, exhibiting luminosity variations of roughly an order of magnitude over timescales of years (e.g., Ricci et al. 2020). Finally, AGNs in dwarf galaxies may suffer from intrinsic X-ray weakness (e.g., Arcodia et al. 2024). The Chandra X-ray observations obtained as part of this program are fairly shallow. Deeper observations would allow the placement of firmer constraints on the non-detections and, in the cases of detected sources, much better X-ray spectra could provide more insights into the nature of these objects, including their X-ray time variability.

6.5. Notes on Individual Objects

Each galaxy in our sample has a compact radio source with a luminosity strongly suggesting the presence of an AGN (Reines et al. 2020). In this section, we aim to use multi-wavelength observations to help determine if a given AGN resides in its apparent dwarf galaxy host or is a background AGN. In addition to the Chandra and HST observations presented here, we also include information from SDSS spectroscopy (taken from Reines

⁵ Ranges are given for the upper limits since the distances to galaxies in the analyzed sample vary significantly (between 70 and 203 Mpc).

Table 6. Radio Loudness Parameters

ID	log L(5GHz)	log L(4400 Å)	log L(2500 Å)	log R	log R*	$\log R_x$
2	21.91	<18.11	<17.82	>3.80	>4.10	> -1.84
6	20.44	<17.68	<17.35	> 2.77	> 3.10	> -1.54
25	21.07	<18.25	< 17.95	> 2.82	> 3.12	> -1.74
26	21.86	19.91	19.25	1.95	2.62	-2.14
28	21.35	<18.08	<17.79	> 3.27	> 3.57	> -1.84
33	22.23	<18.39	<18.08	> 3.84	>4.15	> -1.14
64^a	21.84	19.25	19.00	2.60	2.84	-3.94
65	21.54	<18.11	<17.70	> 3.43	> 3.83	> -2.14
77	21.52	< 18.35	<18.01	> 3.18	> 3.51	> -1.64
82	20.94	19.46	19.32	1.48	1.61	-1.74
83	21.11	19.27	18.77	1.84	2.34	-2.74
92	21.26	20.45	20.51	0.81	0.75	-2.44

Note—Column 1: Radio luminosity in W Hz $^{-1}$ at 5GHz calculated using the spectral index (α) from Reines et al. (2020) and the relation $S_{\nu} \propto \nu^{\alpha}$. Column 2-3: Optical luminosity in W Hz $^{-1}$ at 4400 Å and 2500 Å, respectively, interpolated from the HST flux measurements. For non-detections in relevant optical filters we report upper limits on the luminosity. Column 4-5: Optical radio-loudness parameters calculated at either 4400 Å (R) or 2500 Å (R*). log R (or log R*) > 1 is considered "radio-loud." For non-detections in relevant optical filters we report lower limits on log R. Column 6: X-ray radio-loudness parameter. log $R_{\rm x} >$ -4.5 is considered "radio-loud". We use 2-10 keV X-ray luminosities listed in Table 3. X-ray non-detections we report lower limits on log $R_{\rm x}$. See text in relevant sections for uncertainties on these values.

et al. 2020) and the VLBA observations of Sargent et al. (2022) at 9 GHz with milliarcsecond resolution. Due to the smaller beam size of VLBA versus VLA, nondetections in the VLBA observations indicate more extended radio emission and lower brightness temperatures. Additional information from the literature is also considered. As discussed above, all the radio-detected AGNs are considered radio-loud compared to their luminosities (or upper limits) at X-ray and optical wavelengths (with the exception of ID 92 in the optical). Table 7 summarizes the multi-wavelength results.

ID 2: This radio source is significantly offset from the optical center of the galaxy (4".9). It has neither an X-ray nor an optical counterpart detected. The galaxy is classified as star-forming in all three narrow-line diagnostic diagrams based on its SDSS optical spectrum. However, the SDSS fiber does not overlap with the radio source. The VLA radio source is detected with the VLBA on parsec scales, and its distance from the photocenter of the dwarf galaxy is consistent with expectations for a background AGN.

ID 6: This radio source is off-nuclear, lying 2".1 from the optical center of the galaxy. The galaxy is classified as star-forming in the [O III]/H β versus [N II]/H α and [S II]/H α diagrams and as a LINER in the [O III]/H β

versus [O I]/H α diagram. However, the SDSS fiber does not overlap with the radio source so these classifications should be taken with caution. The VLA radio source does not have detectable VLBA, X-ray, or optical counterparts and we cannot distinguish between a wandering BH in the dwarf galaxy or a background AGN.

ID 25: This radio source is off-nuclear, lying 2".2 from the optical center of the galaxy. The galaxy is classified as star-forming in the [O III]/H β versus [N II]/H α and [S II]/H α diagrams and it is classified as a Seyfert in the [O III]/H β versus [O I]/H α diagram. However, the SDSS fiber does not overlap with the radio source. The VLA radio source has no VLBA, X-ray nor optical counterpart detected and we cannot distinguish between a wandering BH in the dwarf galaxy or a background AGN.

ID 26: This radio source is an AGN that has a position consistent with the nucleus of the dwarf galaxy. It has both an X-ray and optical counterpart detected in the same location as the radio source. This is the only galaxy in our sample that is classified as an AGN/Seyfert in all three optical narrow emission line ratio diagrams and the SDSS fiber overlaps with the radio, X-ray and optical sources. This object was previously confirmed to be an AGN based on optical emission line ratios and broad $H\alpha$ emission (RGG 9 in Reines et al.

^a The luminosities reported for this object are based on the distance of the dwarf galaxy, not the redshift of the background quasar.

2013), as well as mid-IR colors (ID 2 in Latimer et al. 2021). It was not detected by the VLBA.

This galaxy was previously studied in X-rays by Baldassare et al. (2017), where they found that the 2-10 keV X-ray luminosity versus the galaxy SFR (calculated using ${\rm H}\alpha$ emission measured using a 3''.0 SDSS fiber) exceeded expectations from XRBs and indicated the presence of an AGN. In our work, while we measure a very similar 2-10 keV X-ray luminosity, we also investigate the X-ray spectrum of the galaxy and find that it points towards a SF origin for the X-ray emission or at least a significant SFR component. However, we urge caution here since the X-ray spectrum is of poor quality with a low number of counts.

ID 28: This radio source is offset by 2".7 from the optical center of the galaxy. The galaxy is classified as star-forming in all three optical narrow emission line ratio diagrams based on its SDSS optical spectrum. However, the SDSS fiber does not overlap with the radio source. The radio source does not have a detected X-ray or optical counterpart. This object was detected by the VLBA on parsec scales, and its distance from the center of the dwarf galaxy is consistent with expectations for a background AGN.

ID 33: This radio source is off-nuclear, lying 1."1 from the optical center of the galaxy. It is classified as a star-forming galaxy based on all three optical narrow emission line ratio diagrams based on its SDSS optical spectrum. The radio source is positioned near the edge of the SDSS fiber and the fiber also encompasses the entirety of the dwarf galaxy. The VLA radio source is not detected in X-rays or in the optical, nor is it detected with the VLBA. We cannot distinguish between a wandering BH in the dwarf galaxy or a background AGN.

ID 64: This radio source is off-nuclear, lying 0.9 from the optical center of the galaxy. We detect both a bright HST optical and Chandra X-ray counterpart. Our Palomar spectrum reveals that, in addition to the narrow emission lines originating from the dwarf galaxy at redshift z=0.034, there is also a second component corresponding to an AGN at higher redshift (z=0.761). This strongly suggests the radio source is due to a background AGN. Given this redshift and our measured fluxes, we calculate the following luminosities: $L_{9GHz}=2.6\times10^{39}~{\rm erg~s^{-1}}$, $L_{2-10~{\rm keV}}=7.4\times10^{44}~{\rm erg~s^{-1}}$ and $L_{\rm optical}\sim10^{40}~{\rm erg~s^{-1}}$. While the galaxy is classified as star-forming in the [O III]/Hβ versus [N II]/Hα and [O III]/Hβ versus [S II]/Hα diagrams, it is classified as a Seyfert in the [O III]/Hβ versus [O I]/Hα diagram based

on the SDSS optical spectrum. This background AGN is not detected with the VLBA. However, this background AGN may very well be the detected X-ray source, as its spectrum is consistent with that of a Seyfert-type AGN.

ID 65: This radio source is positioned 2".9 from the optical center of the galaxy. The galaxy is classified as star-forming in the [O III]/H β versus [N II]/H α diagram, as a LINER in the [O III]/H β versus [S II]/H α diagram, and as a Seyfert in the [O III]/H β versus [O I]/H α diagram. However, the SDSS fiber does not overlap with the radio source so these classifications should be taken with caution. The radio source does not have a detected X-ray or optical counterpart. It is detected with the VLBA on parsec scales and is consistent with expectations for a background AGN. Alternatively, Dong et al. (2024) suggest this object could be a persistent radio source (PRS) associated with a fast radio burst (FRB) based on its compact size and host-normalized offset.

ID 77: This radio source is offset, lying 2".2 from the optical center of the galaxy. It is classified as a star-forming galaxy in all three optical narrow emission line ratio diagrams based on the SDSS optical spectra. However, the SDSS fiber does not overlap with the radio source. The VLA radio source has neither an X-ray nor an optical counterpart detected, nor is it detected with the VLBA. We cannot distinguish between a wandering BH in the dwarf galaxy or a background AGN.

ID 82: This radio source has a position consistent with the nucleus of the dwarf galaxy. Both an X-ray and optical counterpart were detected for this radio source, but it was not detected with the VLBA. This object was only detected in the hard X-ray band and is consistent with an obscured AGN. It is classified as a star-forming galaxy in all three optical narrow emission line ratio diagrams based on the SDSS optical spectrum, and the SDSS fiber overlaps with the radio source. Despite the SDSS spectral classification of star-forming and the VLBA non-detection, this object was confirmed to be an AGN by the coronal [Fe X] line, enhanced [O I] emission at the same location of the radio source, and broad $H\alpha$ emission (Molina et al. 2021).

ID 83: This radio source is located in the nucleus of the dwarf galaxy. It has both an X-ray and optical counterpart detected at a sky location consistent with the position of the VLA radio source, but no detection with the VLBA. Its X-ray luminosity and spectrum are consistent with those of an AGN. It is classified as a Seyfert galaxy in the [O III]/H β versus [O I]/H α diagram (and star-forming in the other two diagrams) and the SDSS fiber overlaps with the radio source. There are multiple lines of evidence indicating this galaxy hosts a central AGN.

Table 7. Detection Summary

ID	Position		SDSS Spectra			Chan a	lra X-ray	HST Optical	Previous Work
		$[N II]/H\alpha$	[S II]/H α	[O I]/H α	Overlap	Detected	AGN/ULX	Detected	
(1)	(2)	(3)	(4)	(5)	(6)	(7)	(8)	(9)	(10)
2	Wandering	SF	SF	SF	No	-	-	-	VLBA Bkg AGN
6	Wandering	SF	SF	LINER	Yes	-	-	-	-
25	Wandering	SF	SF	Seyfert	No	-	-	-	-
26	Nuclear	AGN	Seyfert	Seyfert	Yes	X	AGN	X	Confirmed AGN
28	Wandering	SF	SF	SF	No	-	-	-	VLBA Bkg AGN
33	Wandering	SF	SF	SF	Yes	-	-	-	-
64	Wandering	SF	SF	Seyfert	Yes	X	AGN	X	-
65	Wandering	SF	LINER	Seyfert	No	-	-	-	VLBA Bkg AGN
77	Wandering	SF	SF	SF	No	-	-	-	-
82	Nuclear	SF	SF	SF	Yes	X	AGN	X	Confirmed AGN
83	Nuclear	SF	SF	Seyfert	Yes	X	AGN	X	-
92^{a}	Nuclear	-	-	-	-	X	ULX	X	

Note—Column 1: Identification number. Column 2: Whether the radio source is considered wandering or nuclear. Column 3: $[O\ III]/H\beta$ versus $[N\ II]/H\alpha$ classification based on SDSS spectroscopy. Column 4: $[O\ III]/H\beta$ versus $[S\ II]/H\alpha$ classification based on SDSS spectroscopy. Column 5: $[O\ III]/H\beta$ versus $[O\ I]/H\alpha$ classification based on SDSS spectroscopy. Column 6: Whether or not the SDSS fiber overlaps with the radio source. Column 7: Whether or not there is an X-ray detection at any location in the galaxy. Column 8: Likely origin of X-ray emission (see Sec 3.3.2). Column 9: Whether or not there is an optical counterpart to the radio source in all optical filters. Column 10: Any previous results about the radio source. Sargent et al. (2022) provides VLBA data. Reines et al. (2013) and Baldassare et al. (2017) confirm the identity of ID 26. Molina et al. (2021) confirms the identity of ID 82.

ID 92: This radio source is co-located with a giant HII region that is visible in the F680N narrowband image. While the SDSS fiber overlaps with the radio source, the spectrum is unreliable at $H\alpha$ and so we cannot definitively classify this galaxy based on narrow line diagnostics. The VLA radio source is not detected with the VLBA. There is an X-ray detection consistent with the position of the radio source, though there are many other optical sources (i.e., star clusters) that could be counterparts of the X-ray source and the X-ray luminosity is consistent with that of a ULX given the SFR of the galaxy. This object is our only target that is considered radio-quiet relative to its optical luminosity. Reines et al. (2020) also pointed out that the radio source was consistent with an HII region within their uncertainties (see their Figure 6).

Here we leverage our high-resolution HST imaging to revisit the origin of this radio source. The production rate of Lyman continuum photons $(Q_{\rm Lyc})$ can be calculated both from the radio emission (assuming a thermal HII region) and from the H α emission. By comparing these $Q_{\rm Lyc}$ values, we can assess whether or not the radio-based value is greatly in excess of the H α -based value. While some difference could be attributed to ex-

tinction (Reines et al. 2008), a radio-based value more than \sim an order of magnitude larger could indicate the presence of an AGN boosting $Q_{\rm Lyc}$.

We first use the following equation from Condon (1992):

$$\left(\frac{Q_{\rm Lyc}}{\rm s^{-1}}\right) \gtrsim 6.3 \times 10^{52} \left(\frac{\rm T_e}{10^4 \rm K}\right)^{-0.45} \left(\frac{\nu}{\rm GHz}\right)^{0.1} \times \left(\frac{\rm L_{\nu, thermal}}{10^{27} \rm erg \, s^{-1} Hz^{-1}}\right), \tag{2}$$

(with $T_e=10^4$ K) along with the radio spectral luminosity at 9 GHz from Reines et al. (2020) to predict the radio-based estimate of $Q_{\rm Lyc}$.

Then we use the equation below along with the relation between the flux of H α and H β assuming Case B recombination, $F_{H\alpha}/F_{H\beta}=2.73$ (Condon 1992), to again predict $Q_{\rm Lyc}$, but this time using the HST-measured H α flux:

$$\left(\frac{Q_{\rm Lyc}}{\rm s^{-1}}\right) \gtrsim 2.25 \times 10^{12} \left(\frac{\rm T_e}{10^4 \rm K}\right)^{0.07} \left(\frac{\rm L_{H\beta}}{\rm erg \ s^{-1}}\right).$$
 (3)

We calculate $F_{H\alpha}$ using our HST imaging as:

a This galaxy's SDSS spectrum was unreliable at H α so we cannot classify this galaxy based on narrow line diagnostics.

$$F_{H\alpha} = [f_{\text{F680N}} - f_{\text{cont}}^{(H\alpha)}] \Delta \lambda_{\text{F680N}}$$
 (4)

where we estimate $f_{\rm cont}^{({\rm H}\alpha)}$ by interpolating between the two wide band filters in log space and $\Delta\lambda_{\rm F680N}$ is the width of the narrow-band filter.

We find that the radio value is somewhat higher than the H α -based value (by a factor of 5): log $Q_{\rm Lyc,radio} = 54.0~{\rm s}^{-1}$ and log $Q_{\rm Lyc,optical} = 53.3~{\rm s}^{-1}$. The difference between the Lyman continuum flux estimates does not necessarily warrant an interpretation of an AGN origin for the radio emission. We also note that the circular aperture in which the H α emission is measured (r = 0.2) has a similar area as the radio source size (0.24×0.2) . From these Q_{Lyc} values and the relation from Kennicutt (1998), SFR(M $_{\odot}\,\rm{yr}^{-1}) = 1.08 \times 10^{-53} \: Q_{Lyc} \: (s^{-1}),$ we calculate the instantaneous star formation rate surface density as $\sim 100 \text{ M}_{\odot} \text{ yr}^{-1} \text{ kpc}^{-2} \text{ using } Q_{\text{Lyc,optical}}$ and $\sim 400 \text{ M}_{\odot} \text{ yr}^{-1} \text{ kpc}^{-2} \text{ using } Q_{\text{Lyc,radio}}$. While these exceed the maximum starburst intensity limit from Meurer et al. (1997) calculated from UV, $H\alpha$, far-IR and radio continuum emission over a wide redshift range, these values are not completely unprecedented. Diamond-Stanic et al. (2012) study three galaxies with star formation rate surface densities of $\sim 3000~{\rm M_{\odot}~yr^{-1}}$ $\rm kpc^{-2}$. They conclude that these high values are not due to contamination from AGNs and are likely from a short-lived phase of compact, extreme star-formation.

We calculate the implied extinction by comparing the measured H α flux ($F_{\text{H}\alpha,\text{observed}} = 2.11 \times 10^{-13} \text{ erg s}^{-1} \text{ cm}^{-2}$) to that predicted from the radio continuum (Condon 1992):

$$\left(\frac{F_{\rm H\alpha, predicted}}{\rm erg \, s^{-1} cm^{-2}}\right) \sim 0.8 \times 10^{-12} \left(\frac{\rm T_e}{10^4 \rm K}\right)^{-0.59} \times \left(\frac{\nu}{\rm GHz}\right)^{0.1} \left(\frac{\rm S_{\nu, thermal}}{\rm mJy}\right) \tag{5}$$

Using this equation with $S_{9 \rm GHz} = 1.16$ mJy from Reines et al. (2020) and assuming $T_{\rm e} = 10^4$ K, we calculate $F_{\rm H\alpha,predicted} = 1.16 \times 10^{-12}$ erg s⁻¹ cm⁻². The extinction at H α is then given by

$$A_{\text{H}\alpha} = -2.5 \times \log \left(\frac{F_{\text{H}\alpha,\text{observed}}}{F_{\text{H}\alpha,\text{predicted}}} \right)$$
 (6)

and we find $A_{\rm H\alpha}=1.85$ mag. This is within the range of known extragalactic massive star forming regions (Reines et al. 2008) and therefore an AGN is not required to explain the radio luminosity.

7. CONCLUSIONS

We have presented Chandra and HST observations of 12 dwarf galaxies with radio-selected AGNs from Reines et al. (2020) to add to a growing body of follow-up observations (Sargent et al. 2022; Dong et al. 2024) of this sample of (sometimes wandering) massive BHs. We use a series of multi-wavelength analyses to characterize the sources of emission from these galaxies. Our primary findings are summarized below.

- 1. We detect both X-ray and optical counterparts of five radio sources (4 nuclear, 1 off-nuclear), with non-detections for the remaining seven. X-ray luminosities are in the range $L_{2-10~{\rm keV}} \sim 10^{40-42}$ erg s⁻¹ assuming the sources are in the target dwarf galaxies.
- 2. Of the 4 nuclear radio sources with X-ray/optical detections, we find compelling multi-wavelength evidence for the presence of AGNs in three of our target dwarf galaxies: IDs 26, 82 and 83. We determine that the other dwarf galaxy may not host a radio AGN at all, as its properties are consistent with an extreme starburst region (ID 92). This object barely made the AGN sample of Reines et al. (2020) and our reanalysis incorporating our HST H α imaging confirms the radio source is consistent with a giant HII region with an extremely high star formation rate surface density ($\sim 100~{\rm M}_{\odot}~{\rm yr}^{-1}~{\rm kpc}^{-2}$). The X-ray source in ID 92 is consistent with a ULX.
- 3. We obtained a Palomar DBSP spectrum of the bright optical counterpart of the off-nuclear radio source towards ID 64 and identify it as a background AGN at z=0.761. The X-ray positional uncertainties prevent us from definitively saying whether or not the X-ray source originates from the background AGN or the target dwarf galaxy.
- 4. Three of the galaxies in our sample have radio AGNs that are detected by the VLBA at parsec scales: IDs 2, 28, and 65. Nevertheless, none have optical or X-ray counterparts. These three radio sources are the most distant from the photocenters of the dwarf galaxies in our sample. Given the interloper modeling presented by Reines et al. (2020) and Sargent et al. (2022), it is likely that these sources are background AGNs and are unrelated to their target dwarf galaxies.
- 5. Four other galaxies in our sample have offset radio AGNs. However, we cannot distinguish between wandering massive BHs in the target dwarf galaxies and background AGNs for these objects (IDs 6, 25, 33, and 77). None of them have detected X-ray or optical counterparts, nor are they detected at

- radio wavelengths on parsec scales with the VLBA (Sargent et al. 2022).
- 6. While we do not detect optical counterparts for all but one (ID 64) of the off-nuclear radio sources, we find that the possible hosts could simply be below our HST detection limits. In the case of wandering BHs, they may be hosted by stellar clusters fainter than our sensitivity limits. For example, we would not detect a 100 Myr-old cluster with a stellar mass below $\sim 10^{6.2} M_{\odot}$.

Identifying the origin of the off-nuclear radio sources towards these galaxies may only be possible using the exquisite capabilities of the James Webb Space Telescope (JWST). Sensitive, high-resolution observations with JWST would allow us to distinguish between any potential stellar overdensities (e.g., the core of a disrupted dwarf galaxy or a star cluster) affiliated with the radio source and residing within the dwarf galaxy (at $z\approx 0$) from a background galaxy/AGN at higher redshift. If the presence of "wandering BHs" is verified, it would confirm predictions from simulations that massive BHs need not always reside in the nuclei of dwarf galaxies (Bellovary et al. 2019) and have important consequences for constraining BH seed formation using dwarf galaxies.

We thank Lilikoi J. Latimer for her preliminary work on the X-ray analysis in this paper and the referee for helpful comments. Support for this work was provided by NASA through Chandra Award No. GO2-23076X issued by the Chandra X-ray Observatory Center, which is operated by the Smithsonian Astrophysical Observatory for and on behalf of the NASA under contract NAS8-03060. Based on observations with the NASA/ESA Hubble Space Telescope obtained from MAST at the Space Telescope Science Institute, which is operated by the Association of Universities for Research in Astronomy, Incorporated, under NASA contract NAS5-26555. Support for Program numbers HST-GO-16843.001-A and HST-GO-16661.001-A were provided through grants from the STScI under NASA contract NAS5-26555. AER acknowledges support provided by NASA through EPSCoR grant number 80NSSC20M0231 and the NSF through CAREER award 2235277. The work of DS and portions of the work of TC were carried out at the Jet Propulsion Laboratory, California Institute of Technology, under a contract with NASA. AB, RK and TC acknowledge support from the Smithsonian Institution and the Chandra Project through NASA contract NAS8-03060. The National Radio Astronomy Observatory is a facility of the National Science Foundation operated under cooperative agreement by Associated Universities, Inc.

REFERENCES

Anglés-Alcázar, D., Faucher-Giguère, C.-A., Quataert, E., et al. 2017, MNRAS, 472, L109

Arcodia, R., Merloni, A., Comparat, J., et al. 2024, A&A, 681, A97

Baldassare, V. F., Reines, A. E., Gallo, E., & Greene, J. E. 2017, The Astrophysical Journal, 836, 20

Baldwin, J. A., Phillips, M. M., & Terlevich, R. 1981, PASP, 93, 5

Becker, R. H., White, R. L., & Helfand, D. J. 1995, ApJ, 450, 559

Begelman, M. C., Volonteri, M., & Rees, M. J. 2006, MNRAS, 370, 289

Bellovary, J. M., Cleary, C. E., Munshi, F., et al. 2019, MNRAS, 482, 2913

Bellovary, J. M., Governato, F., Quinn, T. R., et al. 2010, ApJL, 721, L148

Bellovary, J. M., Hayoune, S., Chafla, K., et al. 2021, MNRAS, 505, 5129 Blecha, L., Cox, T. J., Loeb, A., & Hernquist, L. 2011, MNRAS, 412, 2154

Bogdán, Á., Goulding, A. D., Natarajan, P., et al. 2024, Nature Astronomy, 8, 126

Bond, J. R., Arnett, W. D., & Carr, B. J. 1984, ApJ, 280, 825

Bonning, E. W., Shields, G. A., & Salviander, S. 2007, ApJL, 666, L13

Bromm, V., & Larson, R. B. 2004, ARA&A, 42, 79

Capelo, P. R., Volonteri, M., Dotti, M., et al. 2015, MNRAS, 447, 2123

Condon, J. J. 1992, Annual Review of Astronomy and Astrophysics, 30, 575

Deller, A. T., & Middelberg, E. 2014, AJ, 147, 14

Dev, A., Schlegel, D. J., Lang, D., et al. 2019, AJ, 157, 168

Diamond-Stanic, A. M., Moustakas, J., Tremonti, C. A., et al. 2012, ApJL, 755, L26

- Dong, Y., Eftekhari, T., Fong, W., et al. 2024, ApJ, 973, 133
- Flesch, E. W. 2023, The Open Journal of Astrophysics, 6, 49
- Fruscione, A., McDowell, J. C., Allen, G. E., et al. 2006, in Society of Photo-Optical Instrumentation Engineers (SPIE) Conference Series, Vol. 6270, Society of Photo-Optical Instrumentation Engineers (SPIE)
 Conference Series, ed. D. R. Silva & R. E. Doxsey, 62701V
- Fryer, C. L., Woosley, S. E., & Heger, A. 2001, ApJ, 550, 372
- Gültekin, K., Nyland, K., Gray, N., et al. 2022, MNRAS, 516, 6123
- Habouzit, M., Volonteri, M., & Dubois, Y. 2017, MNRAS, 468, 3935
- Habouzit, M., Volonteri, M., Latif, M., Dubois, Y., & Peirani, S. 2016, MNRAS, 463, 529
- Haiman, Z., & Loeb, A. 2001, ApJ, 552, 459
- Hao, C.-N., Kennicutt, R. C., Johnson, B. D., et al. 2011, The Astrophysical Journal, 741, 124
- Herenz, E. C., Micheva, G., Weilbacher, P. M., et al. 2023, Research Notes of the American Astronomical Society, 7, 99
- HI4PI Collaboration, Ben Bekhti, N., Flöer, L., et al. 2016, A&A, 594, A116
- Ho, L. C. 2008a, ARA&A, 46, 475
- —. 2008b, ARA&A, 46, 475
- —. 2009, ApJ, 699, 626
- Ho, L. C., Filippenko, A. V., & Sargent, W. L. 1995, ApJS, 98, 477
- Jarrett, T. H., Masci, F., Tsai, C. W., et al. 2013, The Astronomical Journal, 145, 6
- Kaaret, P., Feng, H., & Roberts, T. P. 2017, ARA&A, 55, 303
- Kellermann, K. I., Sramek, R., Schmidt, M., Shaffer, D. B., & Green, R. 1989, AJ, 98, 1195
- Kennicutt, R. C., & Evans, N. J. 2012, Annual Review of Astronomy and Astrophysics, 50, 531
- Kennicutt, Jr., R. C. 1998, ARA&A, 36, 189
- Kimbro, E., Reines, A. E., Molina, M., Deller, A. T., & Stern, D. 2021, ApJ, 912, 89
- Kotulla, R., Fritze, U., Weilbacher, P., & Anders, P. 2009, MNRAS, 396, 462
- Kovács, O. E., Bogdán, Á., Natarajan, P., et al. 2024, ApJL, 965, L21
- Kyritsis, E., Zezas, A., Haberl, F., et al. 2025, A&A, 694, A128
- Latimer, L. J., Reines, A. E., Hainline, K. N., Greene, J. E., & Stern, D. 2021, ApJ, 914, 133

- Lehmer, B. D., Eufrasio, R. T., Basu-Zych, A., et al. 2021, ApJ, 907, 17
- Loeb, A., & Rasio, F. A. 1994, ApJ, 432, 52
- Ma, L., Hopkins, P. F., Ma, X., et al. 2021, MNRAS, 508, 1973
- Magorrian, J., Tremaine, S., Richstone, D., et al. 1998, The Astronomical Journal, 115, 2285
- Maiolino, R., Scholtz, J., Witstok, J., et al. 2024, Nature, 627, 59
- Merritt, D., Milosavljević, M., Favata, M., Hughes, S. A., & Holz, D. E. 2004, ApJL, 607, L9
- Meurer, G. R., Heckman, T. M., Lehnert, M. D., Leitherer, C., & Lowenthal, J. 1997, AJ, 114, 54
- Miller, B. P., Brandt, W. N., Schneider, D. P., et al. 2011, ApJ, 726, 20
- Miller, B. P., Gallo, E., Greene, J. E., et al. 2015, ApJ, 799, 98
- Miller, M. C., & Hamilton, D. P. 2002, MNRAS, 330, 232
- Molina, M., Reines, A. E., Latimer, L. J., Baldassare, V., & Salehirad, S. 2021, ApJ, 922, 155
- Moretti, A., Campana, S., Lazzati, D., & Tagliaferri, G. 2003, ApJ, 588, 696
- Nagar, N. M., Falcke, H., Wilson, A. S., & Ho, L. C. 2000, ApJ, 542, 186
- Pettini, M., & Pagel, B. E. J. 2004, MNRAS, 348, L59
- Portegies Zwart, S. F., & McMillan, S. L. W. 2002, ApJ, 576, 899
- Pucha, R., Juneau, S., Dey, A., et al. 2025, ApJ, 982, 10
- Reines, A. E. 2022, Nature Astronomy, 6, 26
- Reines, A. E., Condon, J. J., Darling, J., & Greene, J. E. 2020, The Astrophysical Journal, 888, 36
- Reines, A. E., Greene, J. E., & Geha, M. 2013, The Astrophysical Journal, 775, 116
- Reines, A. E., Johnson, K. E., & Goss, W. M. 2008, The Astronomical Journal, 135, 2222
- Reines, A. E., Plotkin, R. M., Russell, T. D., et al. 2014, The Astrophysical Journal Letters, 787, L30
- Reines, A. E., Reynolds, M. T., Miller, J. M., et al. 2016, The Astrophysical Journal Letters, 830, L35
- Reines, A. E., Sivakoff, G. R., Johnson, K. E., & Brogan,
 C. L. 2011, Nature, 470, 66 EP
- Reines, A. E., & Volonteri, M. 2015, The Astrophysical Journal, 813, 82
- Ricarte, A., & Natarajan, P. 2018, MNRAS, 481, 3278
- Ricci, C., Kara, E., Loewenstein, M., et al. 2020, ApJL, 898, L1
- Richards, G. T., Myers, A. D., Gray, A. G., et al. 2009, ApJS, 180, 67
- Sacchi, A., Bogdán, Á., Chadayammuri, U., & Ricarte, A. 2024, ApJ, 974, 14

- Salehirad, S., Reines, A. E., & Molina, M. 2022, ApJ, 937, 7
 Sargent, A. J., Johnson, M. C., Reines, A. E., et al. 2022, ApJ, 933, 160
- Schleicher, D. R. G. 2018, arXiv e-prints, arXiv:1807.06055
- Schneider, D. P., Hall, P. B., Richards, G. T., et al. 2007, AJ, 134, 102
- Schneider, D. P., Richards, G. T., Hall, P. B., et al. 2010, AJ, 139, 2360
- Schneider, R., Ferrara, A., Natarajan, P., & Omukai, K. 2002, ApJ, 571, 30
- Shen, Y., Richards, G. T., Strauss, M. A., et al. 2011, ApJS, 194, 45
- Swartz, D. A., Soria, R., & Tennant, A. F. 2008, The Astrophysical Journal, 684, 282
- Taffoni, G., Mayer, L., Colpi, M., & Governato, F. 2003, MNRAS, 341, 434
- Terashima, Y., & Wilson, A. S. 2003, The Astrophysical Journal, 583, 145
- Thuan, T. X., & Izotov, Y. I. 2005, ApJS, 161, 240
- Tremmel, M., Governato, F., Volonteri, M., Pontzen, A., & Quinn, T. R. 2018a, ApJL, 857, L22

- Tremmel, M., Governato, F., Volonteri, M., & Quinn, T. R. 2015, MNRAS, 451, 1868
- Tremmel, M., Governato, F., Volonteri, M., Quinn, T. R., & Pontzen, A. 2018b, MNRAS, 475, 4967
- van Wassenhove, S., Volonteri, M., Walker, M. G., & Gair, J. R. 2010, MNRAS, 408, 1139
- Visbal, E., Haiman, Z., & Bryan, G. L. 2014, MNRAS, 445, 1056
- Vito, F., Brandt, W. N., Yang, G., et al. 2018, MNRAS, 473, 2378
- Volonteri, M. 2010, The Astronomy and Astrophysics Review, 18, 279
- Volonteri, M., Lodato, G., & Natarajan, P. 2008, MNRAS, 383, 1079
- Volonteri, M., & Natarajan, P. 2009, MNRAS, 400, 1911
- Volonteri, M., & Perna, R. 2005, MNRAS, 358, 913
- Volonteri, M., & Reines, A. E. 2016, ApJL, 820, L6
- Wilms, J., Allen, A., & McCray, R. 2000, ApJ, 542, 914

APPENDIX

A. X-RAY SPECTRA

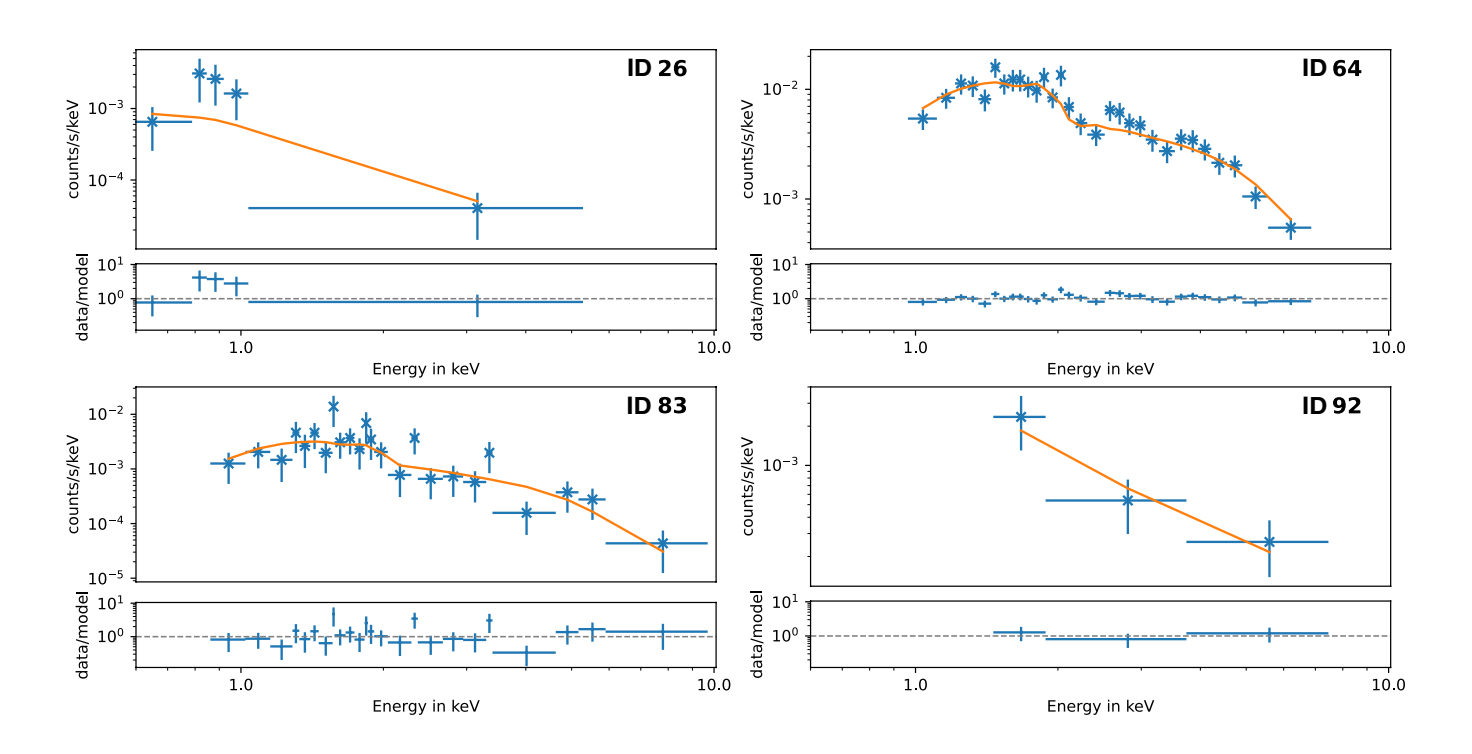


Figure 4. Observed Chandra X-ray spectra with sufficient counts for spectral modeling, best fit power law model (orange line) and ratio residuals. The data have been rebinned for plotting. The simple power law model with fixed Galactic absorption describes IDs 64, 83, and 92 well, but the spectral shape of ID 26 hints at the presence of a feature at $\sim 0.9 \, \text{keV}$.